Research Square

Preprints are preliminary reports that have not undergone peer review.
They should not be considered conclusive, used to inform clinical practice,
or referenced by the media as validated information.

Tuning Fatty Acid-Templated Mesoporous Silica for Adsorption and Hemocompatibility

Oumaima Difallah

Université des Sciences et de la Technologie d'Oran Mohamed Boudiaf

Hadj Hamaizi

hamaizimizou@yahoo.fr

Université Oran 1 Ahmed Ben BellaD

Research Article

Keywords: Mesoporous silica, Sol–gel synthesis, Fatty acid templating, Green chemistry, Biomolecule adsorption, Blood purification

Posted Date: November 26th, 2026

DOI: https://doi.org/10.21203/rs.3.rs-11725599/v1

License: This work is licensed under a Creative Commons Attribution 4.0 International License.
Read Full License

Additional Declarations: No competing interests reported.

Abstract

Mesoporous silica was synthesized via a green sol–gel route using biosourced C16–C18 fatty acid mixtures as structure-directing agents. Tuning the silica precursor, solvent, and pH allowed precise control over the interfacial self-assembly, shifting the template state from encapsulated free fatty acids (acidic) to saponified soap micelles (basic). The optimized fumed silica/NaOH sample (ST4) exhibited exceptional textural properties, featuring a high surface area (958 $m^2 \cdot g^{-1}$), large pore volume (0.89 $cm^3 \cdot g^{-1}$), and a predominantly mesoporous character (79%) with a highly ordered hexagonal structure. This tailored architecture enabled efficient, balanced adsorption of small blood biomolecules (urea, creatinine, and glucose) while demonstrating excellent hemocompatibility (< 3% hemolysis, ISO 10993-4). These findings highlight the potential of eco-friendly, fatty acid-templated mesoporous silica as a highly effective and biocompatible platform for blood purification and biomedical applications.

1. Introduction

Mesoporous silica materials have attracted considerable attention in colloid and interface science due to their exceptional textural properties, including high specific surface areas, tunable pore architectures, and versatile surface chemistry [**1–3**]. These physicochemical characteristics make them highly suitable for a wide range of interfacial applications, from catalysis and separation processes to drug delivery and biomedical devices [**4–8**]. The performance of these materials in such applications is fundamentally governed by their surface properties and mesostructural organization, which are critically dependent on the colloidal self-assembly mechanisms and interfacial chemistry occurring during their synthesis [**9,10**].

The sol–gel process represents a powerful colloidal route for synthesizing mesoporous silica, relying on the hydrolysis and condensation of silicon alkoxides (e.g., tetraethyl orthosilicate, TEOS) in the presence of structure-directing agents [**11,12**]. The introduction of amphiphilic templates during the sol–gel transition enables the formation of highly ordered mesoporous frameworks through cooperative self-assembly at the organic–inorganic interface [**13,14**]. Conventional templates typically include cationic surfactants, such as cetyltrimethylammonium bromide (CTAB) for MCM-41 type materials [**15**], or non-ionic triblock copolymers (e.g., Pluronic P123, F127) for SBA-15 structures [1**6,17**]. While highly effective in controlling pore geometry, these synthetic surfactants present significant drawbacks in terms of cytotoxicity, environmental impact, and high cost, which limit their use in sensitive biomedical and eco-friendly applications [**18,19**].

In this context, the development of sustainable templating strategies based on natural colloidal systems has become a major research focus. Long-chain natural fatty acids (C16–C18), such as stearic, palmitic, and oleic acids, have emerged as promising green alternatives to conventional surfactants [**20,21**]. In aqueous or alcoholic media, under specific pH and temperature conditions, these fatty acids self-assemble into micellar structures or bilayer phases, directing the condensation of silica species around these organized supramolecular assemblies [**22,23**]. The use of fatty acids offers several distinct advantages: (i) they are biosourced, biodegradable, and inherently biocompatible; (ii) their carboxylate

headgroups interact strongly with silica precursors via electrostatic and hydrogen-bonding interactions, facilitating interfacial templating; and (iii) they enable fine-tuning of the surface hydrophobicity and pore size through variations in chain length and degree of unsaturation [**24,25**].

Despite these advantages, most studies on fatty acid-templated mesoporous silica have focused on single-component templates [**26,27**]. The use of biosourced fatty acid mixtures, which form complex mixed-micellar systems, remains largely unexplored. Such mixtures may provide enhanced flexibility in controlling mesostructural organization due to complex intermolecular interactions and altered phase behaviors at the interface [**28**]. Furthermore, the influence of key sol–gel parameters—including the nature of the silica precursor (molecular vs. colloidal), solvent polarity, and catalyst type (acidic vs. basic)—on the micellar organization and the resulting surface properties has not been systematically investigated for fatty acid-templated systems [**29,30**].

Understanding these structure–property relationships is particularly crucial for applications involving biological interfaces, where the hemocompatibility and adsorption performance of mesoporous silica are strongly influenced by surface chemistry, pore size distribution, and morphological features [**31,32**]. For instance, in blood purification and extracorporeal circuits, materials must exhibit low hemolytic activity while efficiently adsorbing target metabolites such as urea, creatinine, and glucose [**33,34**]. The interactions at the blood-material interface—such as protein corona formation, erythrocyte adhesion, and membrane disruption—are directly dictated by the physicochemical properties of the silica surface engineered during the colloidal synthesis [**35,36]**. However, the link between the sol–gel templating parameters, the resulting mesostructural features, and the hemocompatibility remains poorly understood for fatty acid-templated silicas.

In this work, we report the synthesis of mesoporous silica materials using a biosourced mixture of C16–C18 fatty acids via both acid- and base-catalyzed sol–gel routes. The influence of synthesis parameters —including silica source, solvent composition, and catalyst type—on the colloidal self-assembly, mesostructural ordering, and textural properties was systematically investigated. Adsorption experiments toward small biomolecules (creatinine, urea, and glucose) were conducted using human plasma, and hemocompatibility was evaluated according to ISO 10993-4 standards. The main objective was to establish clear structure–property relationships linking the physicochemical conditions of the sol–gel process to the interfacial surface properties, adsorption performance, and hemocompatibility, thereby providing guidelines for the rational design of eco-friendly, functional interfaces for biomedical applications.

2. Materials and Methods

2.1. Materials

A biosourced technical-grade stearic acid mixture (Copoleo™ Stearic Acid, Technical Grade T-703, IOI Oleochemical) was used as the colloidal structure-directing agent. This mixture contained stearic acid

(C18:0, 40–50%), palmitic acid (C16:0, 45–55%), oleic acid (C18:1, 2–5%), and minor fatty acids (C14:0, C18:2, 1–3%), with impurities < 1%. The amphiphilic nature of these long-chain fatty acids, featuring a hydrophilic carboxylate headgroup and a hydrophobic aliphatic tail, makes them ideal candidates for micellar self-assembly at the organic–inorganic interface.

Tetraethyl orthosilicate (TEOS, ≥ 99%) was used as the molecular silica precursor, while fumed silica and colloidal silica (Ludox®, 40 wt.%) served as alternative colloidal silica sources to investigate the effect of precursor type on interfacial templating. Hydrofluoric acid (HF, 40 wt.%), hydrochloric acid (HCl, 37%), and sodium hydroxide (NaOH) were purchased from Sigma-Aldrich and used as catalysts to control the sol–gel interfacial chemistry. All reagents were used without further purification.

2.2. Synthesis of Hybrid Silica–Fatty Acid Materials

Four hybrid silica–fatty acid materials, denoted ST1–ST4, were synthesized using different silica precursors and reaction media to investigate the influence of colloidal and interfacial parameters on the self-assembly process.

For ST1, 5 g of the fatty acid mixture was dispersed in 30 mL of deionized water at 40°C under magnetic stirring (500 rpm) for 1 h, allowing the formation of micellar structures in the aqueous medium. Separately, 9 g of TEOS was hydrolyzed in 30 mL of acidified water (pH ≈ 2, adjusted with HCl) for 2 h, promoting the formation of silanol species. The hydrolyzed silica sol was then added dropwise to the fatty acid dispersion and maintained at 40°C under continuous stirring for 30 min, facilitating interfacial interactions between the silica precursors and the micellar templates. Subsequently, 10 mL of ethanol and 0.5 mL of concentrated HF (40 wt%) were added to induce gelation through acid-catalyzed condensation at the organic–inorganic interface. The resulting gel was aged at 100°C for 72 h in a sealed Teflon container to promote structural organization.

ST2 was prepared following the same procedure as ST1, except that ethanol was used as the solvent instead of water during the initial fatty acid dispersion step. The use of ethanol modified the solvent polarity and the critical micelle concentration, thereby influencing the micellar organization and interfacial templating efficiency.

For ST3, 0.5 g of colloidal silica (Ludox®) was dispersed in 25 mL of ethanol at 55°C, while 10 g of fatty acid mixture was dissolved separately in 25 mL of ethanol at 68°C. The two solutions were mixed under vigorous stirring, and 2 M NaOH was added dropwise until pH ≈ 10. The alkaline conditions induced in situ saponification of the fatty acids into sodium carboxylates (soaps), which formed anionic micellar templates at the interface. The mixture was maintained at 100°C for 24 h under reflux, air-dried for one week at room temperature, and ground into a fine powder.

ST4 was synthesized according to the same procedure as ST3, replacing colloidal silica with fumed silica (Aerosil® 200). The use of fumed silica, consisting of primary nanoparticles with high surface area, was expected to enhance interfacial interactions with the soap micelles and promote a more ordered mesostructural organization.

No calcination treatment was applied to any sample prior to thermal analysis and FTIR characterization in order to preserve the hybrid organic–inorganic interfacial structure. However, all samples intended for XRD, SEM, TEM, and N_2 physisorption analyses were calcined at 550°C for 6 h (heating rate: 2°C·min⁻¹) under air atmosphere to remove the organic template and expose the mesoporous silica framework.

2.3. Material Characterization

The structural, textural, and surface properties of the synthesized materials were investigated using a comprehensive suite of characterization techniques to probe the colloidal self-assembly and interfacial phenomena.

Thermal analysis (TGA-DTA): Thermogravimetric analysis coupled with differential thermal analysis was performed using a SETARAM TG-DTA 92 instrument. Approximately 12 mg of the dried sample was heated from room temperature to 600°C at a heating rate of 10°C·min⁻¹ under air atmosphere (flow rate: 20 mL·min⁻¹). This technique was used to evaluate the thermal stability of the organic–inorganic interface and quantify the organic template content.

Fourier-transform infrared (FTIR) spectroscopy: FTIR spectroscopy was carried out on a PerkinElmer Spectrum 100 spectrophotometer in the transmission mode over the wavenumber range of 4000–400 cm⁻¹ using the KBr pellet technique. Spectra were recorded with a resolution of 4 cm⁻¹ and averaged over 32 scans. This technique was used to characterize the surface chemistry and bonding environments at the organic–inorganic interface, including silanol groups, siloxane bonds, and carboxylate functionalities.

Low-angle X-ray diffraction (XRD): Low-angle XRD patterns were recorded at room temperature on a Philips PW1730 diffractometer equipped with a Cu Kα radiation source (λ = 1.5406 Å). Data were collected over a 2θ range of 0.5–10°. This technique was used to probe the mesostructured ordering and determine the periodicity of the pore arrangement resulting from colloidal templating.

Scanning electron microscopy (SEM): The morphology and surface topography of the samples were examined by SEM using a FE-SEM (JEOL JSM-6340F) operated at an accelerating voltage of 20–30 kV. This technique provided direct visualization of the macro- and mesostructured features arising from the interfacial self-assembly process.

Transmission electron microscopy (TEM): For internal structure analysis, TEM images were recorded on a JEOL JEM-2010 microscope at an accelerating voltage of 200 kV. Samples for TEM were prepared by embedding the silica powder in an epoxy resin, followed by ultramicrotomy to obtain ultrathin sections (~ 50 nm). This technique was used to directly visualize the mesoporous architecture and assess the degree of long-range ordering at the nanoscale.

N_2 physisorption: N_2 adsorption–desorption isotherms were measured at 77 K using a Micromeritics ASAP 2020 automated analyzer. Prior to analysis, the samples were degassed under vacuum at 400°C for 2 h. The specific surface area was calculated using the Brunauer-Emmett-Teller (BET) model in the

relative pressure (P/P_0) range of 0.05–0.30. The pore size distribution was determined from the desorption branch of the isotherm using the Barrett-Joyner-Halenda (BJH) method, applying the Halsey equation for multilayer thickness (± 0.2–0.3 nm). The total pore volume was estimated from the amount of nitrogen adsorbed at a relative pressure of P/P_0 = 0.99. This technique was used to quantitatively evaluate the textural properties and confirm the mesoporosity resulting from colloidal templating.

2.4. Adsorption Experiments at the Biological Interface

Adsorption experiments were performed using human plasma obtained under approved ethical protocols to evaluate the performance of the mesoporous silica at the biological interface. Blood samples were centrifuged to separate plasma, which was used immediately.

Silica samples (50 mg) were added to 1.0 mL plasma and incubated at 37°C under agitation (150 rpm). After defined times (20–60 min), samples were centrifuged and supernatants analyzed. Creatinine, urea, and glucose concentrations were quantified using standard colorimetric assays. Adsorption performance was evaluated from concentration decrease, providing insights into the interaction between the mesoporous surface and blood-borne solutes.

2.5. Hemolysis Assay (Blood-Material Interface Evaluation)

Hemocompatibility was evaluated according to ISO 10993-4 standards to assess the blood-material interface interactions. Materials (10 mg) were incubated with 1 mL diluted human blood at 37°C for 1 h. The samples were then centrifuged at 3000 rpm for 10 min, and the supernatants were measured at 540 nm.

The hemolysis percentage was calculated using the following formula:

$$\%\ \text{Hémolyse} = \frac{\text{Abs}_{\text{sample}} - \text{Abs}_{\text{negative}}}{\text{Abs}_{\text{positive}} - \text{Abs}_{\text{negative}}} \times 100$$

where Abs negative and Abs positive correspond to the absorbance of the negative control (blood in saline) and positive control (blood in distilled water), respectively. This assay provides a quantitative measure of the erythrocyte membrane disruption at the blood-material interface, serving as a critical indicator of hemocompatibility.

3. Results and Discussion

3.1. Thermal Analysis (TGA-DTA): Probing the Organic–Inorganic Interface

Thermogravimetric analysis coupled with differential thermal analysis (TGA-DTA) was performed to evaluate the thermal stability of the organic–inorganic interface and to quantify the organic template

content within the hybrid frameworks (Fig. 1).

The TEOS-based samples (ST1 and ST2) exhibited markedly different thermal behaviors depending on the solvent polarity, which governs the interfacial miscibility. ST1 (aqueous medium) showed a limited total mass loss of 21%, indicating poor interfacial integration of the hydrophobic fatty acids within the hydrophilic silica sol, leading to phase segregation. In contrast, ST2 (ethanol medium) displayed a substantial mass loss of 63%, with two distinct exothermic events (320°C and 450°C). This confirms that the modified solvent polarity facilitated the formation of a highly integrated hybrid interface, effectively encapsulating the fatty acid supramolecular assemblies within the silica matrix.

The basic-synthesized samples (ST3 and ST4) exhibited a fundamentally different thermal signature. Instead of exothermic combustion peaks, an endothermic event was observed around 250–260°C, accompanied by a mass loss of 25–28%. This thermal behavior is characteristic of the decomposition of sodium carboxylates (soaps) formed by the in situ saponification of fatty acids at the alkaline interface (pH ≈ 10). The absence of combustion peaks confirms that the anionic carboxylate headgroups strongly interacted with the silica precursors, forming a stable interfacial ionic network that decomposes into sodium carbonate rather than burning. These results demonstrate that the pH of the reaction medium critically dictates the chemical state of the colloidal template at the organic–inorganic interface.

3.2. FTIR Spectroscopy: Surface Chemistry and Interfacial Bonding

The as-synthesized ST2 sample exhibited characteristic absorption bands corresponding to both the condensed silica network (asymmetric and symmetric Si–O–Si stretching at 1080 and 800 cm^{-1}) and the encapsulated fatty acids [**37,38**]. The presence of the organic phase was evidenced by intense aliphatic C–H stretching vibrations (2920 and 2850 cm^{-1}) and a C = O stretching band at 1710 cm^{-1}, characteristic of protonated carboxylic acid groups (Fig. 2). The broad absorption band between 3000–3500 cm^{-1} corresponded to overlapping O–H stretching vibrations from surface silanol groups (Si–OH) and interfacial hydrogen bonding with the carboxylic acids [**38**].

After calcination at 550°C, the complete disappearance of the C–H and C = O bands confirmed the total removal of the organic template, exposing a highly hydroxylated silica surface. The significant reduction of the O–H band intensity and the sharpening of the Si–O–Si bands reflected the extensive dehydroxylation and condensation of the silica network at high temperatures [**38**]. Notably, the basic-synthesized samples (ST3, ST4) exhibited a shifted C = O band at 1560 cm^{-1} in their as-synthesized state, characteristic of the carboxylate group ($R–COO^-$). This spectroscopic evidence further confirms the saponification mechanism and the formation of strong electrostatic interactions between the anionic soap templates and the cationic silica species at the interface.

Figure 2. FTIR spectra of ST2 before (red) and after (blue) calcination at 550°C, showing the silica network bands (1080, 800 cm^{-1}) and the organic template bands (2920, 2850, 1710 cm^{-1}) before

calcination, and their complete removal after calcination.

3.3. Low-Angle XRD : Mesostructural Ordering via Colloidal Templating

XRD patterns of the calcined samples are shown in Fig. 3. The observed low-angle reflections are characteristic of highly ordered mesoporous structures with periodic pore arrangements, similar to those first reported for MCM-41 type materials [**1,15**]. The large d-spacings correspond to the center-to-center distances between adjacent mesopores, indicating that the fatty acid/soap micelles successfully directed the interfacial condensation of the silica species via the cooperative organization mechanism proposed by Huo et al. [**14**]. The degree of structural coherence varied significantly with the synthesis parameters:

ST4 (fumed silica/NaOH) exhibited the sharpest reflections (FWHM: 0.030°–0.080°), indicating a highly coherent, long-range ordered hexagonal mesostructure (p6mm symmetry), analogous to the seminal MCM-41 and SBA-15 materials [**39,40**]. The high surface area of the fumed silica nanoparticles likely promoted optimal interfacial packing of the soap micelles.

ST1 and ST2 (TEOS/HF) displayed broader peaks, suggesting moderate ordering. The rapid acid-catalyzed gelation kinetics likely restricted the time available for the micellar templates to reorganize into a highly ordered colloidal liquid crystal phase [**14**].

ST3 (colloidal silica/NaOH) showed intermediate peak sharpness, indicating good mesoporosity but slightly less structural perfection than ST4, likely due to the steric hindrance imposed by the pre-formed colloidal Ludox® particles during the self-assembly process.

3.4. Scanning Electron Microscopy (SEM): Surface Morphology and Topography

The surface morphology and topography of the calcined samples were investigated by SEM (Fig. 4), providing direct visual evidence of the macro- and mesostructural features arising from the interfacial self-assembly.

The TEOS-based samples exhibited distinct morphologies dictated by the solvent. ST1 displayed a dense, compact microstructure with limited visible porosity, consistent with the poor interfacial templating efficiency observed in TGA. In contrast, ST2 exhibited a more open, textured morphology, reflecting the successful formation of a hybrid organic–inorganic network prior to template removal, similar to the structures observed in early mesoporous silica syntheses [**40,41**].

A more pronounced morphological divergence was observed for the basic-synthesized samples. ST3 showed the typical morphology of aggregated colloidal nanoparticles forming compact clusters with limited interparticle voids. Conversely, ST4 presented a highly porous, open, three-dimensional network

composed of interconnected nanoscale chains. This highly accessible surface topography creates an abundant macro-/mesostructural arrangement, which is in excellent agreement with its exceptional textural properties and confirms ST4 as the most efficiently structured material in terms of interfacial accessibility. The cooperative self-assembly mechanism at the organic–inorganic interface, as described by Monnier et al. [**42**], likely promoted the formation of this highly ordered and accessible mesoporous architecture.

These SEM observations confirm that the choice of silica precursor and synthesis medium critically influences the final surface morphology and porosity, with fumed silica in basic conditions (ST4) yielding the most favorable interfacial characteristics for mesoporous applications.

3.5. Transmission Electron Microscopy (TEM): Nanoscale Architecture and Interfacial Ordering

TEM micrographs (Fig. 5) provided direct visualization of the nanoscale architecture and the mesoporous ordering inferred from XRD, allowing us to probe the local interfacial arrangement of the silica framework.

ST1 exhibited a relatively dense microstructure with poorly defined porosity, confirming the limited mesostructural ordering and poor colloidal templating efficiency in the aqueous medium. In contrast, ST2, ST3, and ST4 all displayed characteristic honeycomb-like patterns, corresponding to hexagonal arrays of mesopores viewed along the channel axis. This distinct morphological feature is a hallmark of highly ordered mesoporous silica, as first established in seminal works on silicate mesostructures [**40,41**].

ST2 showed well-defined cylindrical channels arranged in locally ordered domains. However, the ordering was limited to short-range distances, consistent with the broader XRD peaks, indicating that the rapid acid-catalyzed gelation restricted the long-range reorganization of the micellar templates. ST3 exhibited a particulate morphology with thicker pore walls, consistent with the aggregation of pre-formed colloidal Ludox® particles which imposed steric hindrance during the self-assembly process.

Finally, ST4 displayed the most highly ordered and continuous honeycomb lattice, with uniform cylindrical pores (diameter ≈ 3.3 nm) arranged in well-defined hexagonal arrays extending over hundreds of nanometers. This exceptional nanoscale ordering visually confirms the optimal interfacial templating achieved with fumed silica and soap micelles. The formation of such a highly coherent, long-range ordered structure is driven by the cooperative self-assembly mechanism at the organic–inorganic interface, where the inorganic silica species condense around the supramolecular micellar templates with minimal structural defects [**16,42**]. This perfect nanoscale architecture directly explains the high specific surface area and the predominantly mesoporous volume of ST4, making it an ideal candidate for interfacial applications.

3.6. N_2 Physisorption: Textural Properties and Interfacial Accessibility

N_2 adsorption–desorption isotherms were recorded to quantitatively evaluate the textural properties and confirm the mesoporosity resulting from colloidal templating (Fig. 6). All four samples exhibited Type IV isotherms with H1 hysteresis loops, characteristic of mesoporous materials according to IUPAC classification [**43,44,47**]. The high nitrogen uptake at relative pressures $P/P_0 > 0.8$ indicated the presence of large mesopores or textural macroporosity.

The BET specific surface areas, pore volumes, and pore size distributions are summarized in Table 1. The BET method was used to calculate specific surface areas [**45**], and the BJH method was applied to determine pore size distributions from the desorption branch [**46**]. A strong correlation was observed between the colloidal synthesis parameters and the resulting textural properties.

ST4 displayed the highest BET surface area (958 $m^2 \cdot g^{-1}$) and the largest total pore volume (0.89 $cm^3 \cdot g^{-1}$). Crucially, the microporous contribution was minimal (102 $m^2 \cdot g^{-1}$, 0.19 $cm^3 \cdot g^{-1}$), indicating that the porosity was essentially mesoporous in nature (0.70 $cm^3 \cdot g^{-1}$ of mesoporous volume, representing 79% of the total pore volume). The pore size distribution revealed a narrow peak centered at 3.59 nm. These exceptional textural properties were fully consistent with the sharp XRD reflections and the open morphology observed by SEM and TEM, confirming that the fumed silica/soap interfacial system assembled into a highly accessible, well-ordered mesoporous network. These values are comparable to those reported for highly ordered mesoporous silicas such as MCM-41 and SBA-15 [**48,4,17**].

ST2 exhibited a moderate total pore volume (0.77 $cm^3 \cdot g^{-1}$) but a significantly lower surface area (720 $m^2 \cdot g^1$) with a substantial microporous contribution (480 $m^2 \cdot g^{-1}$, 0.54 $cm^3 \cdot g^{-1}$), indicating a less optimized mesostructure (mesoporous volume: 0.23 $cm^3 \cdot g^{-1}$, representing ~ 30% of the total pore volume). ST1 showed an intermediate pore volume (0.72 $cm^3 \cdot g^{-1}$) dominated by microporosity (594 $m^2 \cdot g^{-1}$, 0.54 $cm^3 \cdot g^{-1}$), reflecting poor mesoscale templating in the aqueous medium (mesoporous volume: 0.18 $cm^3 \cdot g^{-1}$). Similar improvements in textural properties have been reported for mesoporous silica synthesized using fatty acids as green templates [**18,20,23**].

ST3 exhibited the lowest total pore volume (0.55 $cm^3 \cdot g^1$) with a high microporous surface area (567 $m^2 \cdot g^{-1}$, 0.30 $cm^3 \cdot g^{-1}$), resulting in a limited mesoporous volume of 0.25 $cm^3 \cdot g^{-1}$. This significant microporous contribution is characteristic of silica frameworks synthesized from colloidal precursors, where the pre-formed Ludox® nanoparticles create a highly textured surface with abundant micropores at interparticle contacts, limiting the development of accessible mesoporosity.

Overall, the physisorption data confirms that the fumed silica/NaOH route (ST4) provides the optimal interfacial conditions for maximizing mesoporous volume and surface accessibility, which is critical for mass transport in interfacial applications.

Table 1
Textural properties of mesoporous silica samples (ST1–ST4) determined from N_2 adsorption–desorption analysis; microporous surface areas and pore volume are given in parentheses.

Sample	Mesostructure type	D_{p-p} (nm)	S_{BET} ($m^2.g^{-1}$)	V_p ($cm^3.g^{-1}$)	Average diameter (nm)	% meso
ST1	Disordered / Microporous	7.31	801 (594)	0.72 (0.54)	3.29	~ 25%
ST2	Short-range hexagonal	7.75	720 (480)	0.77 (0.54)	3.58	~ 30%
ST3	Worm-like / Particulate	6.83	882 (567)	0.55 (0.30)	3.66	~ 45%
ST4	Highly ordered hexagonal	7.80	958 (102)	0.89 (0.19)	3.59	~ 79%

3.7. Hemocompatibility: Blood-Material Interface Interactions

The hemocompatibility of the synthesized materials was evaluated by measuring hemolytic activity upon contact with human blood, a critical assessment of the blood-material interface interactions (Table 2). The hemolysis percentage decreased progressively from ST1 (6.8%) to ST4 (2.7%), indicating that the optimization of the surface topography and mesostructural ordering significantly enhances hemocompatibility.

According to ISO 10993-4 standards, materials with hemolysis below 5% are considered hemocompatible [**49**]. ST1 exhibited moderate hemolytic activity, comparable to conventional unmodified mesoporous silica such as MCM-41 (5–10% hemolysis) [**29,30**]. This is likely due to its dense, irregular surface topography which can mechanically disrupt erythrocyte membranes upon contact [**35**].

In contrast, ST3 and ST4 exhibited excellent hemocompatibility (< 3% hemolysis), classifying them as weakly hemolytic. These values represent a substantial improvement over conventional unmodified mesoporous silica and are comparable to those reported for alkyl-functionalized materials (2–4% hemolysis) [**25,28**]. This substantial improvement can be attributed to several interfacial factors:

The highly ordered, smooth mesoporous surface minimizes mechanical damage to cell membranes.

The basic synthesis conditions likely result in a high density of deprotonated silanol groups ($Si–O^-$) at physiological pH, creating a negatively charged surface that electrostatically repels the negatively charged erythrocyte membranes [**20**].

The highly accessible mesoporous network facilitates the rapid formation of a protective protein corona at the solid-liquid interface, which passivates the surface and prevents direct cell-material contact [**22**].

It is worth noting that while fully passivated or polymer-coated mesoporous silica (e.g., PEGylated or heparin-coated materials) typically show hemolysis below 2% [**8,7**], ST3 and ST4 exhibited slightly higher yet still highly acceptable hemolytic activity without any secondary surface functionalization. These results confirm that the tailored surface properties of ST3 and ST4 make them highly suitable for blood-contacting applications.

Table 2
Hemolysis comparison of mesoporous silica materials

Sample	Surface characteristics	Hemolysis (%)	ISO 10993-4 classification	Reference
ST1	Unmodified silica	6.8	Moderately hemolytic	This work
ST2	Partially modified	4.8	Slightly hemolytic	This work
ST3	Surface-modified	2.6	Weakly hemolytic	This work
ST4	Surface-modified	2.7	Weakly hemolytic	This work
MCM-41	Unmodified silica	5–10	Moderately hemolytic	[29,30]
SBA-15	Unmodified silica	4–8	Slightly–moderately hemolytic	[29,30]
Alkyl-functionalized MS	C8/C18-grafted silica	2–4	Weakly hemolytic	[20,23]
PEGylated MS	PEG-coated silica	< 2	Non-hemolytic	[8,9]
Heparin-coated MS	Biofunctionalized silica	< 1–2	Non-hemolytic	[25,28]

3.8. Structure–Property Relationship in Biomolecule Adsorption

The adsorption performance of the mesoporous silica was evaluated toward three small blood biomolecules (creatinine, urea, and glucose) to understand the solid-liquid interfacial interactions relevant to blood purification [**50**]. The adsorption capacities differed significantly among the samples after 1 h of contact (Table 3), revealing a clear structure–property relationship governed by the mesostructural organization and surface chemistry.

ST2 exhibited moderate, non-selective adsorption. The restricted pore connectivity and high microporosity limited mass transport, resulting in moderate uptake. ST3 showed the highest creatinine uptake (45–65%), attributed to strong confinement effects within its narrow mesopores and abundant micropores. These confined spaces enhance van der Waals interactions and hydrogen bonding with the larger creatinine molecules at the solid-liquid interface [**5**]. However, its low total mesoporous volume limited the overall adsorption capacity for smaller molecules.

ST4 exhibited the most balanced and efficient adsorption performance, with optimal uptake for urea (52–66%) and glucose (36–54%), alongside high creatinine extraction (36–43%). The highly ordered hexagonal mesostructure, combined with the large mesoporous volume (0.70 $cm^3 \cdot g^{-1}$) and uniform pore size (3.34 nm), provided highly efficient mass transport pathways. This open architecture allows rapid diffusion of biomolecules to the abundant surface silanol groups, which serve as primary adsorption sites via hydrogen bonding and electrostatic interactions [**4,22,37**].

These results highlight that by tuning the colloidal synthesis parameters, the interfacial properties of the mesoporous silica can be precisely engineered to optimize mass transport and surface-solute interactions, making ST4 a highly promising adsorbent for the selective extraction of blood biomolecules.

Table 3
Adsorption of urea, creatinine, and glucose on mesoporous silica materials (1 h contact time)

Sample	Creatinine extracted (%)	Urea extracted (%)	Glucose extracted (%)
ST2	25–23	18–37	19–27
ST3	45–65	40–52	25–31
ST4	36–43	52–66	36–54

4. Conclusion

In this study, mesoporous silica was successfully synthesized via a green sol–gel route using biosourced C16–C18 fatty acids as structure-directing agents. We demonstrated that tuning the silica precursor and reaction pH governs the interfacial templating mechanism, shifting from free fatty acid encapsulation in acidic media to the formation of highly effective anionic soap micelles in basic media.

By optimizing these parameters (using fumed silica/NaOH), we achieved a material with exceptional textural properties: a high BET surface area (958 $m^2 \cdot g^{-1}$), a large pore volume (0.89 $cm^3 \cdot g^{-1}$), and a predominantly mesoporous character (79%) featuring a highly ordered hexagonal architecture. Crucially, this tailored pore structure established a clear structure–property relationship, providing optimal mass transport pathways for the balanced adsorption of small blood biomolecules (urea, creatinine, and glucose) while ensuring excellent hemocompatibility (< 3% hemolysis).

Ultimately, this eco-friendly strategy provides a versatile platform for engineering tailored pore architectures, paving the way for the rational design of advanced porous materials for biomedical and separation applications.

Declarations

Author Contribution

Author ContributionsOumaima Difallah -Characterization, Conceptualization, Methodology, Investigation.Hadj Hamaizi – Supervision, Project administration, Writing – Review & Editing, CorrespondenceCorresponding Author*Dr. Hadj HamaiziDepartment of Chemistry, Université Oran1 Ahmed Ben Bella, Senia Road, PO Box 1524, Oran Menaouer 31000, Algeria, Email: hamaizimizou@yahoo.fr; Tel: +213-550-462417; Fax: +213-41513077 / +213-41416021

Acknowledgement

The authors acknowledge the financial support of the University of Oran 1 and the Public Health Institution of Es-Senia for providing biological samples. Special thanks to Dr. Alik Nezha from EPSP Senia, for her help in conducting the laboratory tests

References

1. C.T. Kresge, M.E. Leonowicz, W.J. Roth, J.C. Vartuli, J.S. Beck, Ordered mesoporous molecular sieves synthesized by a liquid-crystal template mechanism, Nature 359 (1992) 710-712. https://doi.org/10.1038/359710a00
2. M. Vallet-Regí, I. Izquierdo-Barba, A.L. Doadrio, Thermal treatment of MCM-41, Microporous Mesoporous Mater. 48 (2001) 1-8. https://doi.org/10.1016/S1387-1811(01)00298-9
3. A. Corma, Inorganic solid acids and their use in acid-catalyzed hydrocarbon reactions, Chem. Rev. 95 (1995) 559-614. https://doi.org/10.1021/cr00035a009
4. J. Liu, X. Yang, D. Wang, G.Q. Lu, D. Zhao, S.Z. Qiao, Ordered mesoporous polymer-coated hollow spheres for adsorption and catalysis, Adv. Funct. Mater. 17 (2007) 2936-2942. https://doi.org/10.1002/adfm.200601079
5. M. Hartmann, D. Jung, Protein adsorption and release from mesoporous materials, J. Mater. Chem. 20 (2010) 844-857. https://doi.org/10.1039/B917896K
6. M. Vallet-Regí, M. Colilla, A.L. Doadrio, Mesoporous silica nanoparticles for drug delivery, Chem. Soc. Rev. 42 (2013) 3866-3882. https://doi.org/10.1039/C3CS35482E
7. J.M. Rosenholm, V. Mamaeva, C. Sahlgren, M. Lindén, Nanoparticles in targeted cancer therapy: mesoporous silica nanoparticles entering the preclinical development stage, Nanomedicine 7 (2012) 111-120. https://doi.org/10.2217/nnm.11.166
8. A. Popat, S.B. Hartono, F. Stahr, J. Liu, S.Z. Qiao, G.Q. Lu, Mesoporous silica nanoparticles for bioadsorption, enzyme immobilisation, and delivery, Nanoscale 3 (2011) 2801-2818. https://doi.org/10.1039/C1NR10224A
9. V. Cauda, A. Schlossbauer, T. Bein, Bio-degradation study of colloidal mesoporous silica nanoparticles: effect of surface functionalization with organosilanes, Microporous Mesoporous Mater. 132 (2010) 60-71. https://doi.org/10.1016/j.micromeso.2010.01.020

10. I.I. Slowing, J.L. Vivero-Escoto, C.W. Wu, V.S. Lin, Mesoporous silica nanoparticles as controlled release drug delivery and gene transfection carriers, Adv. Drug Deliv. Rev. 60 (2008) 1278-1288. https://doi.org/10.1016/j.addr.2008.03.010
11. C.J. Brinker, G.W. Scherer, Sol-Gel Science: The Physics and Chemistry of Sol-Gel Processing, Academic Press, San Diego, 1990.
12. L.L. Hench, J.K. West, The sol-gel process, Chem. Rev. 90 (1990) 33-72. https://doi.org/10.1021/cr00099a003
13. G.D. Stucky, J.E. MacDougall, Quantum solids and macroscale composite materials, Science 264 (1994) 1109-1111. https://doi.org/10.1126/science.264.5162.1109
14. Huo, Q., Margolese, D.I., Ciesla, U., Feng, P., Gier, T.E., Sieger, P., Leon, R., Petroff, P.M., Schüth, F. and Stucky, G.D. Generalized synthesis of periodic surfactant/inorganic composite materials. Nature 1994;368:317-321.
15. J.S. Beck, J.C. Vartuli, W.J. Roth, M.E. Leonowicz, C.T. Kresge, K.D. Schmitt, C.T.W. Chu, D.E. Olson, E.W. Sheppard, S.B. McCullen, J.B. Higgins, J.L. Schlenker, A new family of mesoporous molecular sieves prepared with liquid crystal templates, J. Am. Chem. Soc. 114 (1992) 10834-10843. https://doi.org/10.1021/ja00053a020
16. Q. Huo, R. Leon, P.M. Petroff, G.D. Stucky, Mesostructure Design with Gemini Surfactants: Supercage Formation in a Three-Dimensional Hexagonal Array, Science 268 (1995) 1324-1327. https://doi.org/10.1126/science.268.5215.1324
17. D. Zhao, J. Feng, Q. Huo, N. Melosh, G.H. Fredrickson, B.F. Chmelka, G.D. Stucky, Triblock copolymer syntheses of mesoporous silica with periodic 50 to 300 Å pores, Science 279 (1998) 548-552. https://doi.org/10.1126/science.279.5350.548
18. D. Kumar, R.K. Singh, P.S. Chauhan, Palmitic acid as a green template for mesoporous silica synthesis, Microporous Mesoporous Mater. 228 (2016) 132-139. https://doi.org/10.1016/j.micromeso.2016.03.021
19. Z. Moradi, A. Ghorbani-Choghamarani, Green preparation and characterization of AGC-ZM-2022 as a novel mesoporous silica material using palmitic acid as a natural template, RSC Adv. 13 (2023) 2265-2268. https://doi.org/10.1039/D2RA07952A
20. X. Li, H. Zhang, L. Wang, Oleic acid templated mesoporous silica: effect of acid/TEOS ratio on porosity, J. Colloid Interface Sci. 505 (2017) 123-131. https://doi.org/10.1016/j.jcis.2017.05.060
21. J. Chen, P. Li, Q. Yang, Ricinoleic acid methyl esters for preparation of stable mesoporous silica structures, Mater. Lett. 142 (2015) 276-280. https://doi.org/10.1016/j.matlet.2014.12.066
22. J. Liu, X. Jiang, C. Ashley, C.J. Brinker, Electrostatically mediated adsorption of proteins on mesoporous silica, J. Am. Chem. Soc. 131 (2009) 7567-7579. https://doi.org/10.1021/ja900734z
23. S. Singh, R. Patel, N. Verma, Stearic acid and C16–C18 fatty acids in the green synthesis of mesoporous silica, Green Chem. 20 (2018) 345-353. https://doi.org/10.1039/C7GC03064A
24. B. Tian, Z. Yang, J. Yu, Influence of surfactants and synthesis conditions on mesostructure formation of silica, Chem. Mater. 20 (2008) 6722-6729. https://doi.org/10.1021/cm801527k

25. H. Wei, L. Han, J. Ren, L. Jia, Anticoagulant surface coating using composite polysaccharides with embedded heparin-releasing mesoporous silica, ACS Appl. Mater. Interfaces 5 (2013) 12471-12478. https://doi.org/10.1021/am403947w
26. E. Elimbinzi, J.E. Mgaya, Mixed bio-based surfactant-templated mesoporous silica for supporting palladium catalyst, Heliyon 10 (2024) e39168. https://doi.org/10.1016/j.heliyon.2024.e39168
27. Y. Li, W. Zhang, Z. Su, Y. Wang, Controlled synthesis of mesoporous silica materials: pore size, wall thickness, and morphology, Microporous Mesoporous Mater. 131 (2010) 123-130. https://doi.org/10.1016/j.micromeso.2009.12.021
28. X. Wu, L. Chen, Y. Zhang, J. Li, Mesoporous silica nanoparticles-encapsulated agarose and heparin as anticoagulant and bacteria-resistant coatings for biomedical silicone, Langmuir 33 (2017) 5245-5252. https://doi.org/10.1021/acs.langmuir.7b00666
29. T. Yu, K. Greish, L.D. McGill, A. Ray, H. Ghandehari, Influence of geometry, porosity, and surface characteristics of silica nanoparticles on hemolytic activity in vitro, ACS Nano 6 (2012) 2289-2301. https://doi.org/10.1021/nn204716y
30. J. Slowik, A. Borkowska, A. Mielcarek, Monitoring the hemolytic effect of mesoporous silica nanoparticles, Eur. J. Inorg. Chem. 2015 (2015) 4595-4602. https://doi.org/10.1002/ejic.201500658
31. T. Yu, A. Malugin, H. Ghandehari, Impact of silica nanoparticle design on cellular toxicity and hemolytic activity, ACS Nano 5 (2011) 5717-5728. https://doi.org/10.1021/nn2007108
32. M. Vallet-Regí, M. Colilla, I. Izquierdo-Barba, M. Manzano, Mesoporous silica nanoparticles for drug delivery: current insights, Molecules 23 (2018) 47. https://doi.org/10.3390/molecules23010047
33. Ordered porous materials for blood purification, Sep. Purif. Technol. 328 (2024) 124965. https://doi.org/10.1016/j.seppur.2023.124965
34. Extraction of blood biomolecules by adsorption onto silica adsorbents, Authorea Preprint (2024). https://doi.org/10.22541/au.170665868.89864124
35. Y. Zhao, Z. Li, L. Zhang, W. Dai, Y. Ding, Hemocompatibility of mesoporous silica nanoparticles: effect of surface charge and particle size, J. Biomed. Mater. Res. A 102 (2014) 3450-3459. https://doi.org/10.1002/jbm.a.35012
36. J. Liu, X. Jiang, C. Ashley, C.J. Brinker, Electrostatically mediated adsorption of proteins on mesoporous silica, J. Am. Chem. Soc. 131 (2009) 7567-7579. https://doi.org/10.1021/ja900734z
37. K.M. Parida, L. Mohapatra, Infrared spectroscopy investigation of the interaction of water with the surface of mesoporous silica, J. Phys. Chem. C 113 (2009) 13458-13465. https://doi.org/10.1021/jp903456x
38. L.T. Zhuravlev, The surface chemistry of amorphous silica. Colloid interface science, Colloids Surf. A Physicochem. Eng. Asp. 173 (2000) 1-38. https://doi.org/10.1016/S0927-7757(00)00556-2
39. D. Zhao, Q. Huo, J. Feng, B.F. Chmelka, G.D. Stucky, Nonionic triblock and star diblock copolymer and oligomeric surfactant syntheses of highly ordered, hydrothermally stable mesoporous silica structures, J. Am. Chem. Soc. 120 (1998) 6024-6036. https://doi.org/10.1021/ja980039o

40. S. Inagaki, Y. Fukushima, K. Kuroda, Synthesis of highly ordered mesoporous materials from a layered polysiloxane, J. Chem. Soc. Chem. Commun. (1993) 680-682. https://doi.org/10.1039/C39930000680
41. T. Yanagisawa, T. Shimizu, K. Kuroda, C. Kato, The preparation of alkyltrimethylammonium-kanemite complexes and their conversion to microporous materials, Bull. Chem. Soc. Jpn. 63 (1990) 988-992. https://doi.org/10.1246/bcsj.63.982
42. A. Monnier, F. Schüth, Q. Huo, D. Kumar, D. Margolese, R.S. Maxwell, G.D. Stucky, M. Janoney, A. Beck, P. Petroff, Cooperative formation of inorganic-organic interfaces in the synthesis of silicate mesostructures, Science 261 (1993) 1299-1302. https://doi.org/10.1126/science.261.5126.1299
43. M. Thommes, K. Kaneko, A.V. Neimark, J.P. Olivier, F. Rouquerol, P.L. Llewellyn, T.P. Binder, L. Moser, F. Rouquerol, D. Rouquerol, K.S.W. Sing, Physisorption of gases, with special reference to the evaluation of surface area and pore size distribution (IUPAC Technical Report), Pure Appl. Chem. 87 (2015) 1051-1069. https://doi.org/10.1515/pac-2014-1117
44. K.S.W. Sing, D.H. Everett, R.A. Haul, L.R. Moscow, R.H. Ottewill, S. Sircar, Reporting physisorption data for gas/solid systems with special reference to the determination of surface area and porosity, Pure Appl. Chem. 57 (1985) 603-619. https://doi.org/10.1351/pac198557040603
45. S. Brunauer, P.H. Emmett, E. Teller, Adsorption of gases in multimolecular layers, J. Am. Chem. Soc. 60 (1938) 309-319. https://doi.org/10.1021/ja01269a023
46. E.P. Barrett, L.G. Joyner, P.P. Halenda, The determination of pore volume and area distributions in porous substances. I. Computations from nitrogen isotherms, J. Am. Chem. Soc. 73 (1951) 373-380. https://doi.org/10.1021/ja01145a126
47. J. Rouquerol, D. Avnir, C.W. Fairbridge, D.H. Everett, J.M. Haynes, N. Pernicone, et al., Recommendations for the characterization of porous solids, Pure Appl. Chem. 66 (1994) 1739-1758. https://doi.org/10.1351/pac199466081739
48. V.S. Lin, C.Y. Lai, J.L. Huang, S.J. Song, C. Cheng, Mesoporous silica nanoparticles for drug delivery and gene transfection, J. Am. Chem. Soc. 123 (2001) 11545-11546. https://doi.org/10.1021/ja016462y
49. International Organization for Standardization, ISO 10993-4: Biological evaluation of medical devices – Part 4: Selection of tests for interactions with blood, ISO, Geneva, 2017.
50. I. Ledebo, C. Ronco, Blood purification in the treatment of acute kidney injury: current concepts and future directions, Blood Purif. 41 (2016) 192-199. https://doi.org/10.1159/000442879

Figures

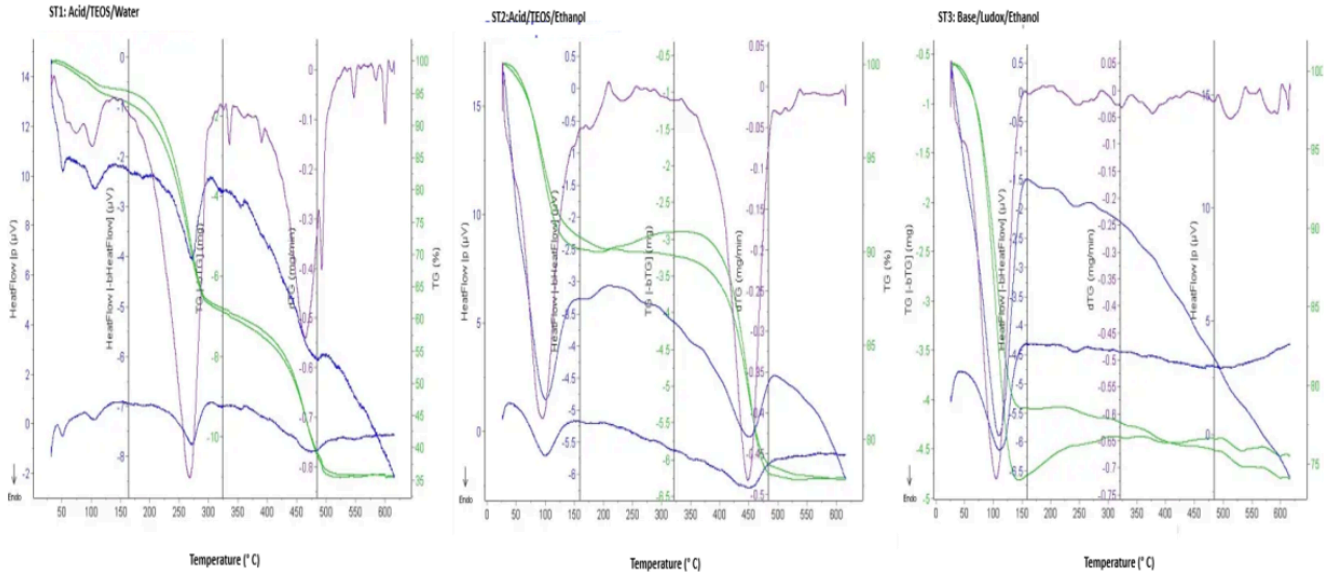


Figure 1

TGA-DTA curves of the hybrid silica–fatty acid materials before calcination: (a) mass loss as a function of temperature for ST1–ST4; (b) corresponding DTA curves showing exothermic (ST1, ST2) and endothermic (ST3, ST4) events.

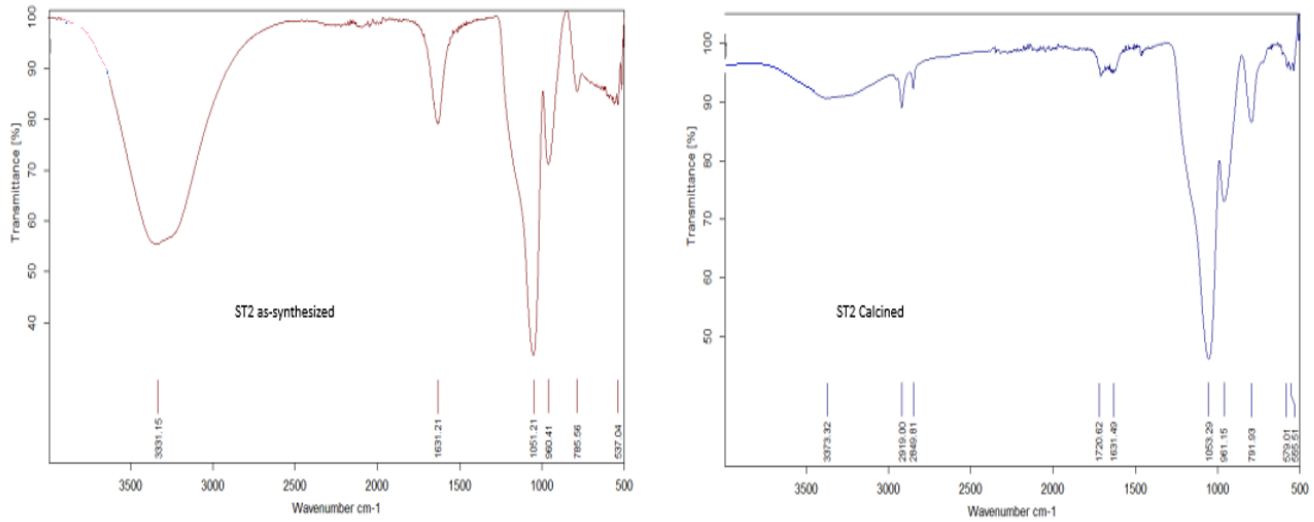


Figure 2

FTIR spectra of ST2 before (red) and after (blue) calcination at 550 °C, showing the silica network bands (1080, 800 cm^{-1}) and the organic template bands (2920, 2850, 1710 cm^{-1}) before calcination, and their complete removal after calcination.

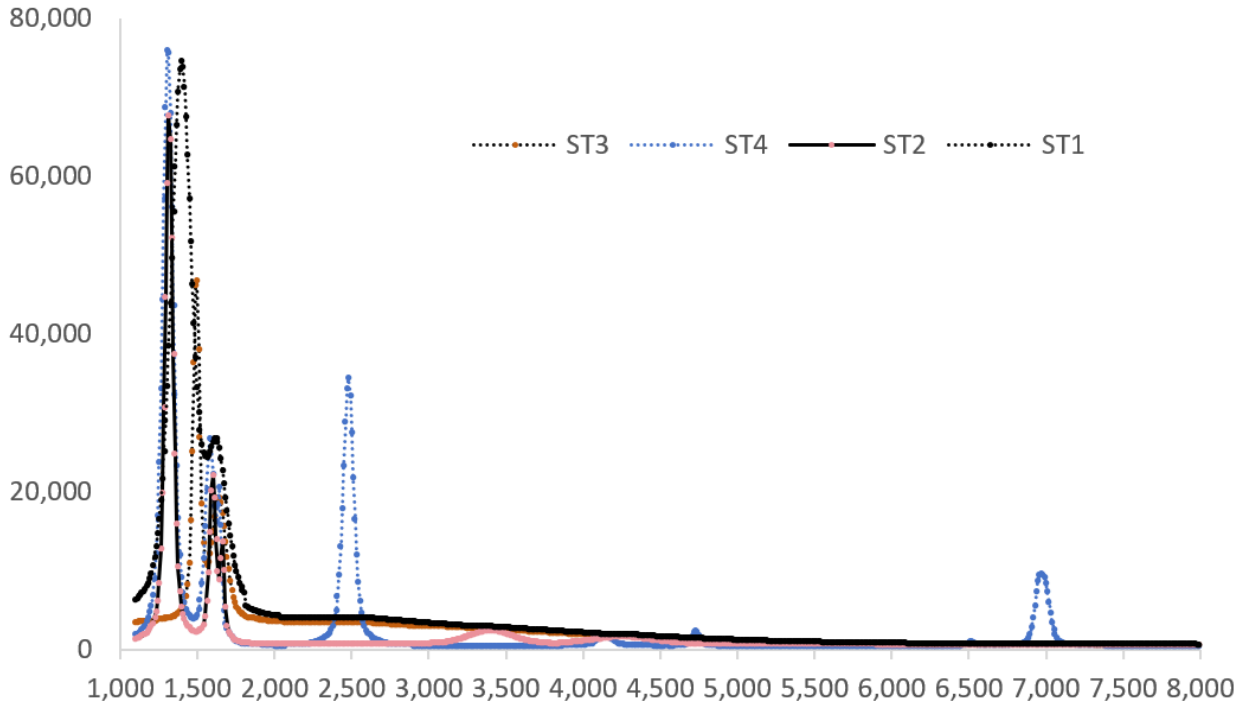


Figure 3

Low-angle XRD patterns of calcined mesoporous silica samples ST1–ST4, showing intense reflections at 2θ = 1.3°–9.2° characteristic of ordered mesoporous structures, with varying degrees of structural ordering.

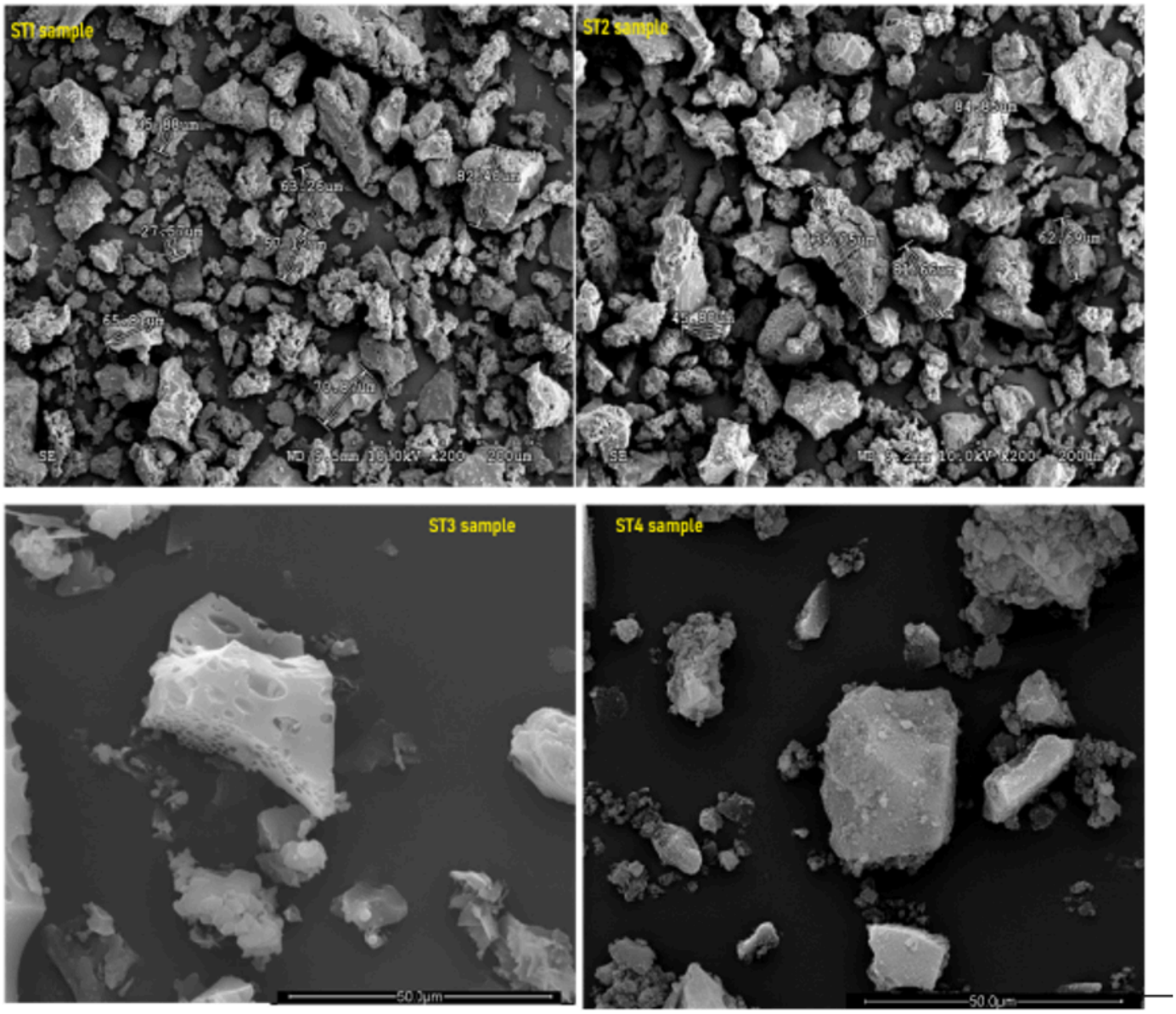


Figure 4

SEM images of calcined mesoporous silica samples: (a) ST1, dense microstructure; (b) ST2, open textured morphology; (c) ST3, aggregated colloidal particles; (d) ST4, highly porous three-dimensional network.

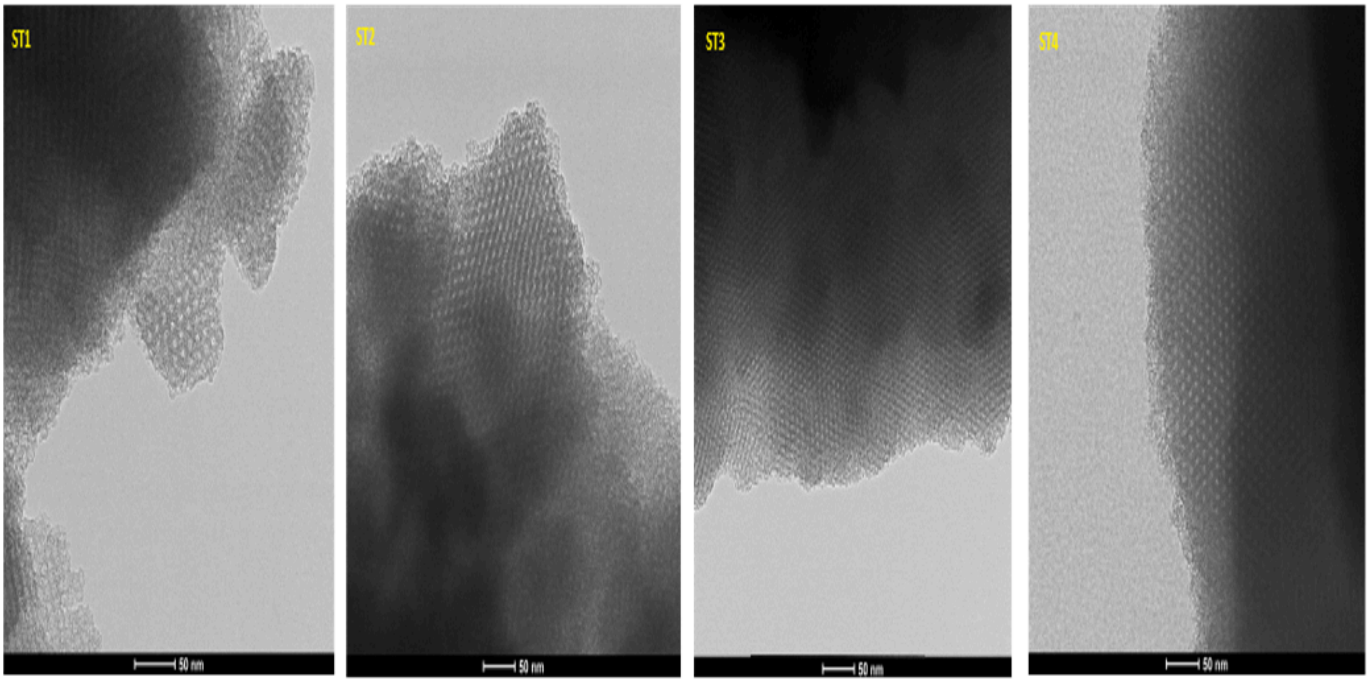


Figure 5

TEM micrographs of calcined mesoporous silica samples: (a) ST1, poorly defined porosity; (b) ST2, hexagonal pore arrays with short-range order; (c) ST3, particulate morphology with thicker walls; (d) ST4, highly ordered hexagonal honeycomb lattice.

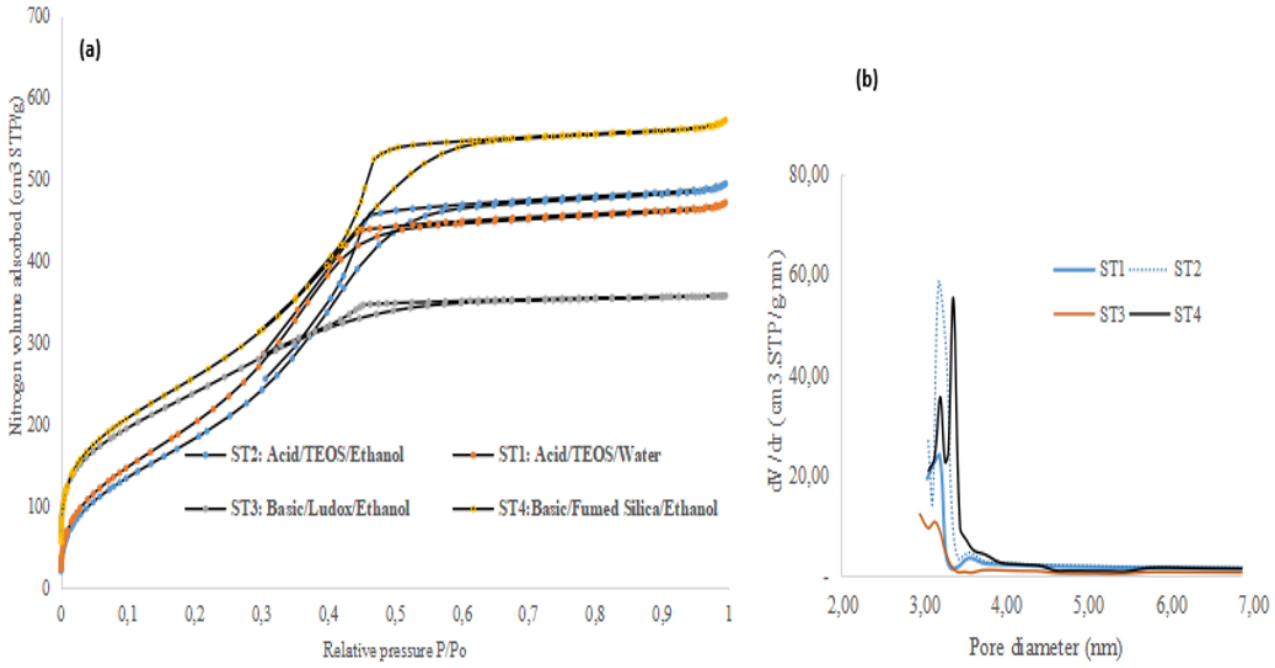


Figure 6

(a) N_2 adsorption–desorption isotherms at 77 K for ST1–ST4, all exhibiting Type IV isotherms characteristic of mesoporous materials; (b) corresponding pore size distributions derived from the desorption branch using the BJH method.